



SenseNet: A Physics-Informed Deep Learning Model for Shape Sensing

Yitao Qiu¹; Prajwal Kammardi Arunachala²; and Christian Linder³

Abstract: Shape sensing is an emerging technique for the reconstruction of deformed shapes using data from a discrete network of strain sensors. The prominence is due to its suitability in promising applications such as structural health monitoring in multiple engineering fields and shape capturing in the medical field. In this work, a physics-informed deep learning model, named SenseNet, was developed for shape sensing applications. Unlike existing neural network approaches for shape sensing, SenseNet incorporates the knowledge of the physics of the problem, so its performance does not rely on the choices of the training data. Compared with numerical physics-based approaches, SenseNet is a mesh-free method, and therefore it offers convenience to problems with complex geometries. SenseNet is composed of two parts: a neural network to predict displacements at the given input coordinates, and a physics part to compute the loss using a function incorporated with physics information. The prior knowledge considered in the loss function includes the boundary conditions and physics relations such as the strain—displacement relation, material constitutive equation, and the governing equation obtained from the law of balance of linear momentum. SenseNet was validated with finite-element solutions for cases with nonlinear displacement fields and stress fields using bending and fixed tension tests, respectively, in both two and three dimensions. A study of the sensor density effects illustrated the fact that the accuracy of the model can be improved using a larger amount of strain data. Because general three dimensional governing equations are incorporated in the model, it was found that SenseNet is capable of reconstructing deformations in volumes with reasonable accuracy using just the surface strain data. Hence, unlike most existing models, SenseNet is not specialized for certain types of elements, and can be extended universally for even thick-body applications. DOI: 10.1061/JENMDT.EMENG-6901. © 2023 American Society

Introduction

Over the last few decades, structural health monitoring (SHM) has been studied extensively by researchers from different communities, such as civil engineering, aerospace engineering, and mechanical engineering (Brownjohn 2007; Giurgiutiu 2016; Xiang et al. 2018). One of the goals of SHM is to detect real-time structural health information to (1) increase human and environmental safety, (2) make structures intelligent and improve maintenance efficiency, and (3) reduce maintenance costs and enhance sustainability. As an emerging technology with interdisciplinary applications, the development of SHM involves sensor technologies (Liang et al. 2009; Shen et al. 2015; Fernando 2005), tracking system deformation (Castro-Toscano et al. 2021), damage identification (Feng and Feng 2018), data analysis, and Internet of things (IoT) (Dervilis et al. 2015; Jo et al. 2018; Arcadius Tokognon et al. 2017). In conventional static structure analysis, the loading information is utilized for computing system deformation. Nevertheless, accurate estimation of the actual applied loads can be difficult in most practical cases. In these scenarios, shape sensing, which refers to a technique for real-time reconstruction of deformed structures using a discrete network of strain sensors, has been found to be significantly important.

In addition to SHM, the shape sensing technique also has promising applications in the field of medicine. One such prominent application is in transtibial prosthetics, wherein shape capturing approaches are in great demand for the creation of a representation of the residual limb (Yang et al. 2019). Currently, the design is either done manually, which is based completely on the prosthetist's skill and experience, or performed computationally based on theoretical models, which have been found to be inaccurate for complex shapes (Yang et al. 2019). Similar to transtibial prosthetics, customized orthopedic casts have been found to notably improve the comfortability and functionality for patients (Rao et al. 2019). In this regard, additive manufacturing is an emerging technology that can be used to print personal orthopedic casts (Kumar et al. 2022), and shape sensing technique can help compute the desired shapes. Therefore, an accurate shape sensing technique which can reconstruct precisely the deformed shapes based on sensor data is essential owing to such significant practical applications.

In general, existing shape sensing approaches can be classified into four categories (Gherlone et al. 2018). The first category is based mostly on Ko's displacement theory, which performs the numerical integration of discrete strain measurements (Ko et al. 2007). The key idea was proposed for beamlike structures, and follow-up work extended the application to wing-boxes and plates (Ko et al. 2007, 2009; Ko and Fleischer 2009; Jutte et al. 2011; Bakalyar and Jutte 2012). The second category approximates the displacement field using global or piecewise continuous basis functions fitted with experimental strain data (Foss and Haugse 1995; Pisoni et al. 1995; Davis et al. 1996; Bogert et al. 2003; Kim and Cho 2004). One of the representative methods of this category is the modal method, which employs normal modes as basis functions to predict the deformation (Foss and Haugse 1995; Pisoni et al. 1995; Bogert et al. 2003). The third category is based on finite-element

¹Graduate Student, Dept. of Civil and Environmental Engineering, Stanford Univ., Stanford, CA 94305. Email: yitaoqiu@stanford.edu

²Graduate Student, Dept. of Civil and Environmental Engineering, Stanford Univ., Stanford, CA 94305. ORCID: https://orcid.org/0000-0002-7891-6786. Email: prajwalk@stanford.edu

³Associate Professor, Dept. of Civil and Environmental Engineering, Stanford Univ., Stanford, CA 94305 (corresponding author). ORCID: https://orcid.org/0000-0002-5731-5631. Email: linder@stanford.edu

Note. This manuscript was submitted on August 7, 2022; approved on November 1, 2022; published online on January 5, 2023. Discussion period open until June 5, 2023; separate discussions must be submitted for individual papers. This paper is part of the *Journal of Engineering Mechanics*, © ASCE, ISSN 0733-9399.

discrete variational principles, one of which is known as the inverse finite-element method (iFEM), which was developed by Tessler and Spangler (2003, 2005). Compared with the aforementioned approaches, the iFEM approach is the most robust and versatile, because it enforces strain-displacement relations in the formulation and enables the reconstruction of deformed shapes without any prior knowledge of loading conditions and material properties (Gherlone et al. 2018; Kefal et al. 2021). Owing to the great advantages of the iFEM approach, further enhancements and extensions to different types of structures such as plates, shells, beams, and frame structures have been explored (Tessler and Spangler 2004; Tessler et al. 2011; Kefal and Oterkus 2015; Kefal et al. 2016; Gherlone et al. 2012, 2014). The experimental validation of the iFEM approach and its applications to realistic scenarios were presented by Quach et al. (2005), Gherlone et al. (2014), and Kefal and Oterkus (2016a, b). The iFEM approach was extended further to multilayered composite and sandwich structures by Cerracchio et al. (2013, 2015), Kefal et al. (2017), and Kefal and Yildiz (2017) using the Refined Zigzag Theory (Tessler et al. 2010). The last category consists of methods based on neural networks (Bruno et al. 1994; Mao and Todd 2008). In contrast to the previous approaches, these models do not consider any physics laws binding the system. However, they require a training data set with input data, such as member length changes, and the corresponding labelled output data, such as the body deformations. Due to the nature of conventional purely data-driven neural networks, the performance of these models relies strongly on the choices of the training data.

Raissi et al. (2019) developed the concept of physics-informed neural networks (PINNs) by incorporating prior knowledge of the problem as soft constraints into the loss function to solve supervised learning tasks. The prior knowledge includes the governing physics laws expressed using partial differential equations, initial conditions, and boundary conditions, which help reduce the solution space of target problems. Thus, PINNs do not require labelled solutions, unlike conventional purely data-driven neural networks, and therefore their performance is not biased by the training data. It has been demonstrated that this framework has great success in solving complex systems such as the Schrödinger equation, the Allen-Cahn equation, the Navier-Stokes equations, and Burgers' equation (Raissi et al. 2019). Following Raissi et al. (2019), extensive efforts have investigated the application of PINNs in other research fields such as fluid mechanics (Cai et al. 2022; Lucor et al. 2021; Sun and Wang 2020; Mahmoudabadbozchelou et al. 2021a, b), solid mechanics (Zhang et al. 2020a, b; Li et al. 2021; Liu et al. 2021; Bahmani and Sun 2021; Zhang and Garikipati 2021), heat transfer problems (Cai et al. 2021), power systems (Huang and Wang 2022), climate modeling (Kashinath et al. 2021), biological applications (Sahli Costabal et al. 2020; Linka et al. 2022), and chemical reactions (Ji et al. 2021). However, the application of this method for shape sensing is lacking in literature.

Because of the prominence of shape sensing technique for interdisciplinary applications, this paper introduces a physics-informed deep learning model, named SenseNet, for reconstructing deformed shapes using sensor data without prior knowledge of the loading information. Inspired by Raissi et al. (2019), SenseNet uses a simple fully connected neural network to compute displacements as the output corresponding to the input coordinates. Using automatic differentiation (Baydin et al. 2018) and physics relations such as the strain–displacement relation and the material constitutive equation, SenseNet is able to compute the corresponding mechanical strain, mechanical stress, and residual of the governing equation obtained from balance of linear momentum. This physics knowledge, along with the boundary conditions, is incorporated during the formulation of the loss function in order to train the model. The model was tested by simulating a bending test as a case with a nonlinear displacement field and a fixed tension test as a case with a nonlinear stress field, in both two and three dimensions. Furthermore, a study of the effects of the amount of sensor data on the performance of the model was conducted for the two-dimensional (2D) simulations. Unlike iFEM (Tessler and Spangler 2003, 2005), SenseNet does not require a mesh, but only the geometry of the continuum. Therefore, SenseNet is a mesh-free approach for shape sensing, with a potential advantage in tackling problems with complex geometries. Because the physics knowledge of the problem is incorporated, its performance is expected to be more robust than the traditional neural network approaches, which are biased depending on the choices of the training data set. Furthermore, unlike most existing approaches, incorporation of the general three-dimensional (3D) governing equations can help the model predict volume deformations utilizing just the surface strain data.

The outline of the paper is as follows. We start by explaining the mechanism of SenseNet and the workflow of the current study using SenseNet in the section "Methods." Numerical examples in 2D and 3D contexts are discussed in the section "Numerical Results for 2D Applications" and section "Numerical Results for 3D Applications," respectively. Because sensor density is one of the primary factors that can affect the results, its effects are studied in the section "Sensor Density Effects." Finally, the SenseNet approach and the numerical results are summarized in the section "Conclusions."

Methods

SenseNet is a physics-informed deep learning model for reconstructing deformed shapes using sensor data without prior knowledge of the loading information. SenseNet consists of two parts (Fig. 1): the neural network and the physics part. The neural network takes the spatial coordinates vector \mathbf{x} as the input and predicts the displacement vector \mathbf{u} at corresponding input coordinates as the output. In a 2D context, $\mathbf{x} = \{x, y\}$, $\mathbf{u} = \{u_x, u_y\}$; in 3D, $\mathbf{x} = \{x, y, z\}$, $\mathbf{u} = \{u_x, u_y, u_z\}$. Using these displacements and utilizing automatic differentiation, the physics part first computes the mechanical strain tensor $\boldsymbol{\varepsilon}$ using the strain–displacement relation given by

$$\boldsymbol{\varepsilon} = \frac{1}{2} (\nabla \boldsymbol{u} + \nabla^{\mathrm{T}} \boldsymbol{u}) \tag{1}$$

Assuming a linear elastic material and utilizing Hooke's law as the material constitutive equation, the mechanical stress tensor is computed as

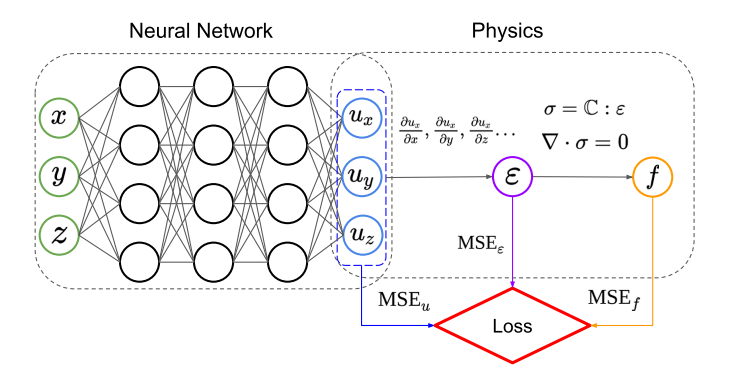


Fig. 1. Schematic diagram of SenseNet with both the neural network and the physics part.

$$\boldsymbol{\sigma} = \lambda \operatorname{tr} \boldsymbol{\varepsilon} \boldsymbol{I} + 2\mu \boldsymbol{\varepsilon} \tag{2}$$

where λ and μ = Lamé's parameters. Further, the residual vector f of the governing equation obtained from the balance of linear momentum is obtained as

$$f = \nabla \cdot \boldsymbol{\sigma} \tag{3}$$

The loss function considered for SenseNet contains three components

$$\mathcal{L} = MSE_u + MSE_{\varepsilon} + MSE_f \tag{4}$$

where MSE_u = mean square error in displacements on fixed boundaries; MSE_ε = mean square error in projected strains compared with strain data at given sensor locations and along predefined directions; and MSE_f = mean square error of residual f of governing equation in the whole domain. In practice, each loss component can be scaled by different weights to balance the total loss.

The first component of the loss function, MSE_u , considers the satisfaction of the fixed boundary conditions, wherein faces, edges, or points can have zero displacement along a particular direction. Assuming that $u^{pred}(x)$ is the component of the predicted displacement, which ideally should be zero at any sampled point x on such fixed boundaries, the mean squared error can be written as

$$MSE_{u} = \frac{1}{N_{u}} \sum_{k=1}^{N_{u}} (u^{\text{pred}}(\mathbf{x}_{k}))^{2}$$
 (5)

where N_u = total number of sampling points over which boundary conditions are applied.

The second component of the loss function, MSE_ε , accounts for the discrepancy between the sensor strain data and the predicted strains at certain locations. Although SenseNet is generalized for different types of sensors, we assume a certain type of sensor pair that can measure strain information along two perpendicular directions. Considering practicality for the purpose of fabrication, each sensor pair is assumed to measure strains along either 0° and 90° , or 45° and 135° , wherein angles are assumed to be measured anticlockwise from the *x*-axis. Using the predicted displacements of the neural network, SenseNet first computes the mechanical strain

tensors ε using Eq. (1) at the locations of the strain sensors. Then SenseNet transforms this strain tensor to a projected scalar strain value $\varepsilon^{\text{pred}}$ along the corresponding direction in which those sensor data are reported. The projected strain along the sensor direction vector t can be computed as

$$\varepsilon^{\text{pred}} = \boldsymbol{t} \cdot \boldsymbol{\varepsilon} \boldsymbol{t} \tag{6}$$

Using this, the mean square error component can be written as

$$MSE_{\varepsilon} = \frac{1}{N_{\varepsilon}} \sum_{k=1}^{N_{\varepsilon}} (\varepsilon_k^{\text{pred}} - \varepsilon_k^{\text{sensor}})^2$$
 (7)

where N_{ε} = total number of strain data points; and $\varepsilon^{\text{sensor}}$ = strain values reported by sensors.

The last component of the loss function is considered to fulfill the balance of linear momentum in the whole domain. The governing equation obtained from the balance law given by

$$\rho \dot{\boldsymbol{v}} = \nabla \cdot \boldsymbol{\sigma} + \rho \boldsymbol{b} \tag{8}$$

is the most fundamental equation of mechanics, describing the mechanical equilibrium of an infinitesimal volume element. In Eq. (8), ρ is the density of the material, \mathbf{v} is the velocity field, and \mathbf{b} is the body force. This paper considers only static and quasi-static problems, and hence neglects the term $\rho\dot{\mathbf{v}}$. In addition, for the sake of simplicity, the body force also is ignored, so Eq. (8) is simplified to obtain

$$\nabla \cdot \boldsymbol{\sigma} = \mathbf{0} \tag{9}$$

For the fulfillment of Eq. (9), the residual vector f is calculated using Eq. (3) and the mean squared error component is defined as

$$MSE_f = \frac{1}{N_f} \sum_{k=1}^{N_f} ||f_k||^2$$
 (10)

where N_f = total number of sampling points in the whole domain; and the L_2 norm is considered.

The work flow of this study is depicted in Fig. 2. Owing to the lack of experimental data, we first ran forward finite-element

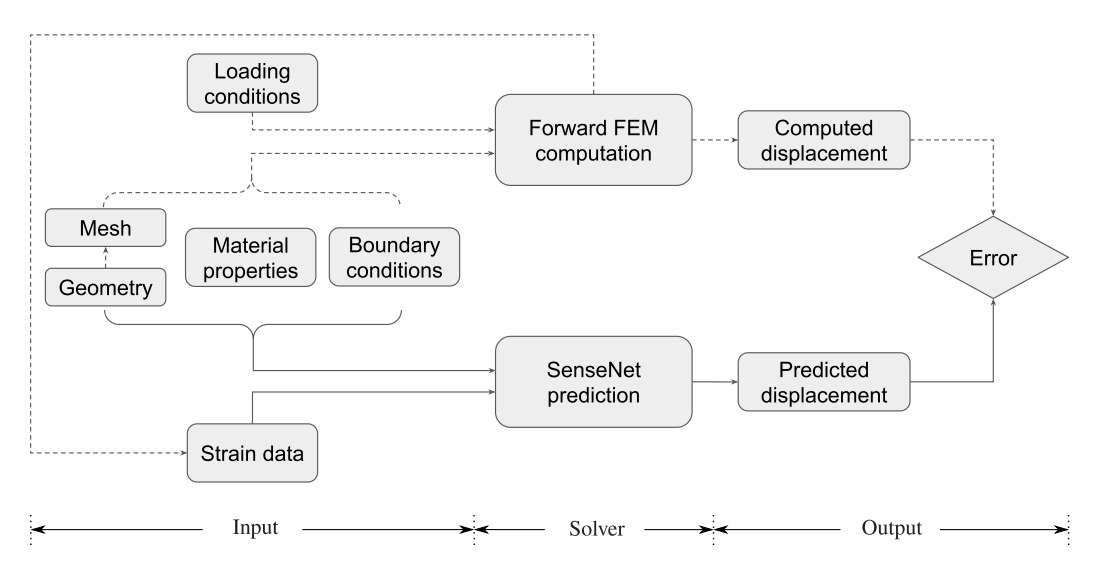


Fig. 2. Work flow for this study.

simulations using the mesh generated from the geometry, material properties, boundary conditions, and loading conditions in order to generate strain and displacement data. SenseNet utilizes these strain data along with the geometry, material properties, and boundary conditions for the training process. Finally, predictions of SenseNet were validated using the displacement data obtained from the forward finite-element simulations. For better visualization, the processes related to the forward finite-element simulations are represented by dashed lines in Fig. 2, whereas the solid lines denote SenseNet-related processes. Unlike traditional numerical methods, SenseNet requires only the geometry of the problem, rather than the mesh generated from the geometry. Therefore, SenseNet is a meshfree method which is convenient for problems with either complex geometry or extremely large deformations.

The accuracy of the predictions of SenseNet was assessed using the normalized RMS error (RMSE) metric (Gherlone et al. 2018; Zhao et al. 2020), which is defined as

normalized RMSE =
$$\frac{\sqrt{\frac{1}{N}\sum_{i=1}^{N}(\|\boldsymbol{u}^{\text{ref}} - \boldsymbol{u}^{\text{pred}}\|^{2})}}{\max(\|\boldsymbol{u}^{\text{ref}}\|)}$$
(11)

The numerator is the RMSE of the predicted displacements u^{pred} with respect to the reference displacements u^{ref} at N different locations. In this work, u^{ref} represents the displacements calculated using forward finite-element simulations, although it also can use experimental measurements if these are available. The denominator is the maximal magnitude of the reference displacements. The magnitudes of the vectors are obtained using the L_2 norm.

Numerical Results for 2D Applications

The ability of SenseNet to reconstruct the deformed shapes using discrete sensor data was verified by performing benchmark simulations and comparing the predicted displacements with the forward finite-element solutions. The schematic diagrams of all these tests are presented in Fig. 3, in which dashed and solid lines represent the outlines of the undeformed and deformed shapes, respectively, and the black strips and dotted lines represent the visible and unseen sensor pairs, respectively. In all our simulations, we assumed E=100 and $\nu=0.4$ as the material parameters. Furthermore, a simple fully connected neural network with 7 hidden layers, with each layer consisting of 20-40 neurons and using the tanh activation function, was used. In practice, we used the Adam optimizer rather than the Broyden-Fletcher-Goldfarb-Shanno (BFGS) optimizer, because the latter was found to be more vulnerable to local minima. Moreover, an exponential learning rate decay is applied in the training of SenseNet, which helps the optimization and generalization of the model. As a multiobjective optimization problem, weights of different loss components need to be adjusted carefully to avoid potential gradient conflict issues. In this work, the weight of MSE_f was set to 1, and the weights of MSE_{μ} and MSE_{ϵ} were set to 10,000 to mitigate the scaling effect of E on MSE_f .

Although most practical applications are 3D in nature, many of these problems can be simplified as 2D problems using assumptions such as plane strain, plane stress, and axisymmetry, which can reduce the computational complexity significantly. Therefore, we first validated SenseNet for different 2D problems by assuming plane strain conditions. Specifically, SenseNet was tested for 2D bending and 2D fixed tension problems in the following two subsections.

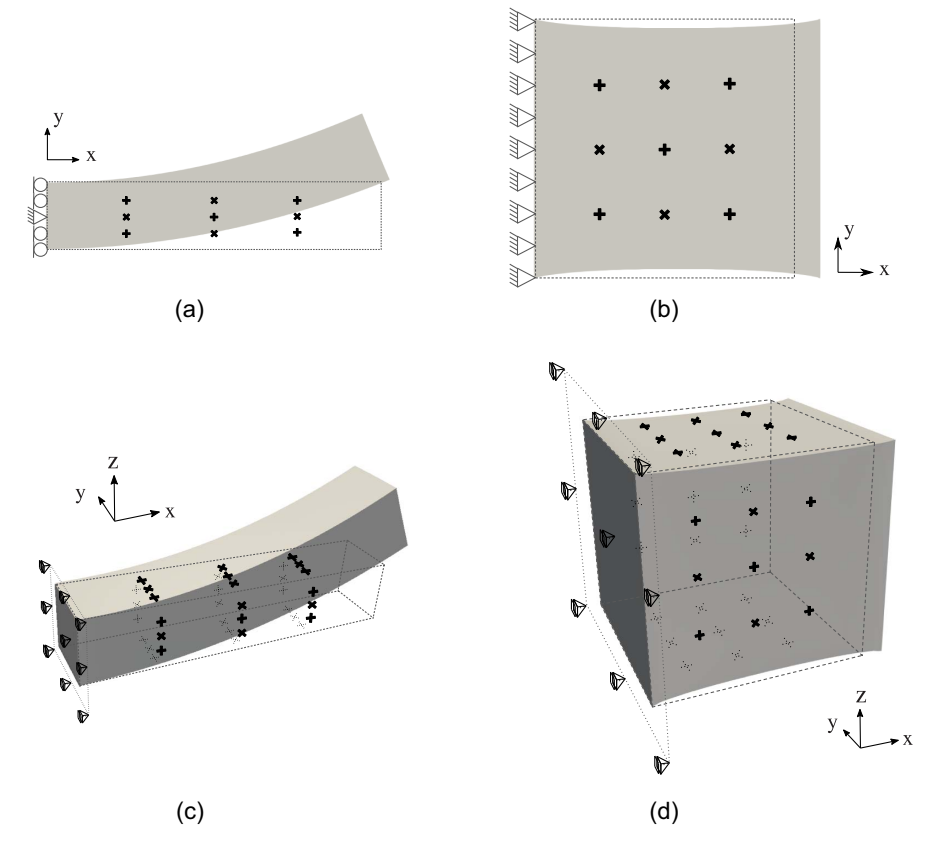


Fig. 3. Schematic diagrams of bending and fixed tension tests in 2D and 3D contexts: (a) 2D bending test; (b) 2D fixed tension test; (c) 3D bending test; and (d) 3D fixed tension test.

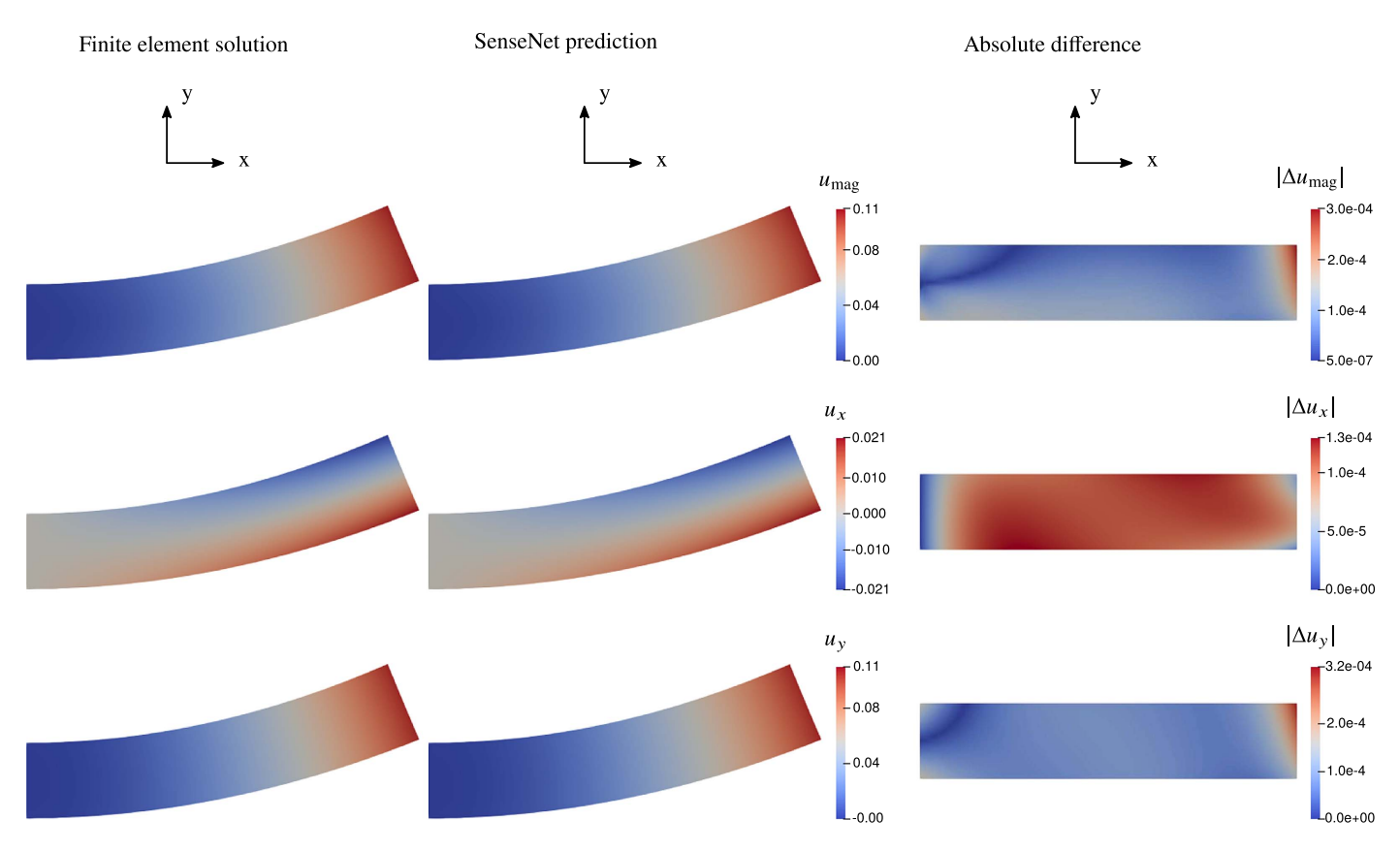


Fig. 4. Comparison of SenseNet prediction with finite-element solution for 2D bending test.

Two-Dimensional Bending Test

To validate if our model is capable of reproducing nonuniform displacement fields, a simple bending test of a 2D beam was performed in this subsection. The domain of the beam was assumed to be within (0,0) and (5,1) [Fig. 3(a)]. Regarding the boundary conditions, the left end of the beam is fixed in the x-direction, implying that $u_x = 0$ at x = 0. In addition, the center point on the left boundary was fixed in both the x- and y-directions, implying that $u_x = u_y = 0$ at x = 0, y = 0.5. In the forward finite-element simulation, the right end of the beam was applied with a moment, which remained unknown to SenseNet. The moment was achieved using a Neumann boundary condition with the distributive traction only along the x-direction as $F_x = 0.5 - y$, where a positive stress value implies a rightward stress and a negative stress value implies a leftward stress.

We assumed that nine sensor pairs were used in this problem, which were located at the intersections of $x = \{1.25, 2.5, 3.75\}$ and $y = \{0.25, 0.5, 0.75\}$. The orientation of each sensor pair was different from that of its neighboring pairs, so that the sensors could capture strain information along different directions.

Fig. 4 plots the contours of the displacement magnitude $u_{\rm mag}$ and the displacement components u_x , u_y obtained by the forward finite-element simulation in the first column on the deformed configuration. The second column plots the deformed shape predicted by SenseNet, with the contours of $u_{\rm mag}$, u_x , and u_y . The deformed shape in these two columns are scaled by a factor of 10 for better visualization. The absolute differences in $u_{\rm mag}$, u_x , and u_y between the finite-element solution and the SenseNet prediction, denoted by $|\Delta u_{\rm mag}|$, $|\Delta u_x|$, and $|\Delta u_y|$, are plotted on the undeformed geometry of the beam in the third column. The deformed shape predicted by SenseNet matched reasonably well with the shape obtained by the

forward finite-element simulation. The maximal absolute differences $|\Delta u_{\rm mag}|$, $|\Delta u_x|$, and $|\Delta u_y|$ all were of the same order of magnitude, 10^{-4} . Because the left boundary was constrained in the x-direction by minimizing the loss, the error in u_x on that boundary was the least. In the y-direction, only the center point of the left boundary (x=0,y=0.5) was fixed, and therefore $|\Delta u_y|$ was the least at that point.

To show the relative accuracy, we define the percentage difference (PD) (Kefal and Oterkus 2016b) as

$$PD = \frac{|\Delta u_i|}{\max|u_i|} \tag{12}$$

where u_i can be u_x , u_y , or u_{mag} . The maximal PDs computed were 0.27% in u_{mag} , 0.62% in u_x , and 0.29% in u_y . The maximal PD was much larger in u_x due to its smaller magnitude, because the main deflection was in the y-direction. Whereas the contour plots of absolute differences exhibit the local accuracy information, the normalized RMSE represents the global accuracy, which was 0.129% for this problem (Table 1).

Table 1. Normalized RMSE and maximal PDs of 2D bending and fixed tension tests (%)

Problems	2D bending	2D fixed tension
Normalized RMSE	0.129	0.934
Maximal PD (u_{mag})	0.27	5.7
Maximal PD (u_x)	0.62	6.6
Maximal PD (u_y)	0.29	13.5

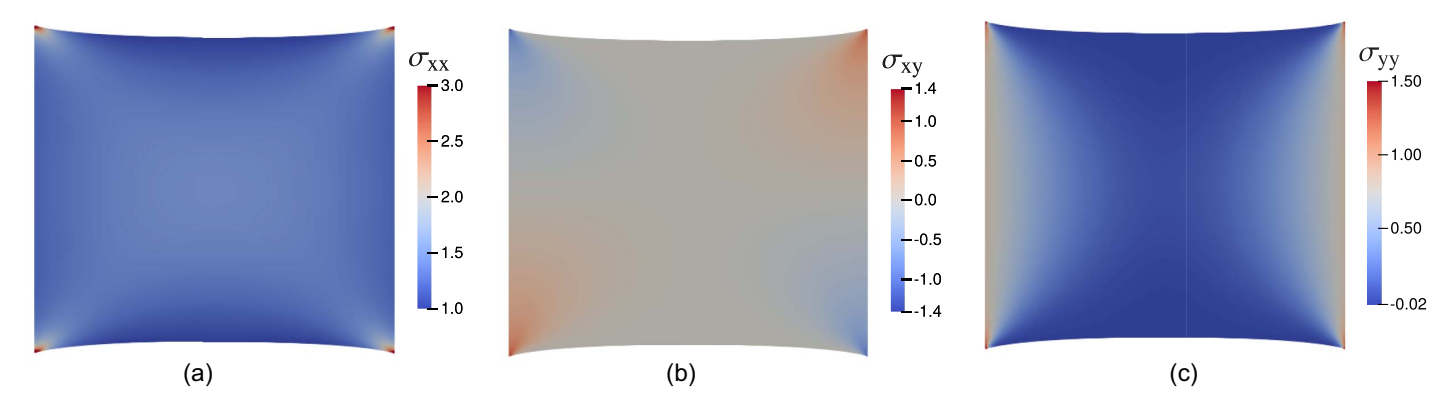


Fig. 5. Stress distributions in 2D fixed tension test: (a) σ_{xx} ; (b) σ_{xy} ; and (c) σ_{yy} .

Two-Dimensional Fixed Tension Test

To validate our model for predicting the deformed shapes for cases with nonlinear stress distributions, a simple fixed tension test was performed on a unit square, the domain of which was within (0,0) and (1,1). The left boundary of the plate was fixed in both the x- and y-directions, whereas the right boundary was fixed only in the y-direction and imposed with a displacement in the x-direction [Fig. 3(b)]. We assumed $u_x = u_y = 0$ at x = 0 for the boundary conditions and $u_x = 0.1$ and $u_y = 0$ at x = 1 for the loading conditions. Both the boundary and loading conditions were known to the forward finite-element simulation, whereas SenseNet was unaware of the loading conditions.

Nine sensor pairs were assumed in this problem, which were located at the intersections of $x = \{0.25, 0.5, 0.75\}$ and $y = \{0.25, 0.5, 0.75\}$ [Fig. 3(b)]. Similar to the previous 2D bending test case, we differed the orientation of each sensor pair from its neighboring pairs to collect more strain information along different directions.

Due to the imposed boundary and loading conditions, there were stress concentrations in the fixed tension test. Stress concentrations arose mainly around the four corners in the contour plots of σ_{xx} , σ_{xy} , and σ_{yy} (Fig. 5). Because calculating the residual of the governing equation in Eq. (3) involves the gradient of each stress component, the stress concentration phenomenon may hinder the performance of the model.

The normalized RMSE for this problem was 0.934% (Table 1), which was higher than that in the 2D bending test. However, the visualization of the deformed shape predicted by SenseNet matched reasonably well with the shape obtained by the forward finite-element simulation (Fig. 6). The first and second columns in Fig. 6 present the contours of u_{mag} , u_x , and u_y on the deformed shapes obtained by the forward finite-element simulation and predicted by SenseNet, respectively. The deformed shapes are scaled by a factor of 10 for better visualization. The contour plots of absolute differences in u_{mag} , u_x , and u_y are presented on the undeformed configuration in the third column. The maximal values of u_{mag} , u_x , and u_y had the same order of magnitude, 10^{-4} . The prediction of SenseNet mostly captured the deformed shape, although there were some differences around the four corners. The left end of the plate remained flat, because a Dirichlet boundary condition was imposed to keep it clamped. However, small curvatures occurred at the top and bottom of the right end of the plate, although it also was expected to be flat. These small curvatures resulted in a smoother stress distribution at the right boundary, and hence it can be one of the consequences resulting from the stress concentrations. The maximal absolute differences in u_{mag} , u_x , and u_y were located at the four corners and the right boundary, which may be caused by the stress concentrations, as explained previously. The maximal PDs were about 5.7% in $u_{\rm mag}$, 6.6% in u_x , and 13.5% in u_y . The larger maximal PD in u_y was due to the fact that $|u_y|$ was much smaller than $|u_x|$ and $u_{\rm mag}$.

These examples show the ability of the model to capture the deformed shapes for cases with nonlinear displacement and stress fields in 2D.

Numerical Results for 3D Applications

The practicality of 3D applications makes it vital to study the behavior of our model for such cases. The reconstruction of the deformed volumes using just the available surface sensor data adds to the complexity of the problem. To validate the performance of SenseNet for 3D applications, we studied similar tests in 3D in this section, specifically, 3D bending and 3D fixed tension tests.

Three-Dimensional Bending Test

Similar to the 2D bending test in the previous section, SenseNet was validated with a 3D beam in a bending test in this subsection. The beam had a length of 5 in the x-direction, a thickness of 1 in the y-direction, and a height of 1 in the z-direction [Fig. 3(c)]. The beam was clamped at the left end, with $u_x = u_y = u_z = 0$ at x = 0, which was the boundary condition for this problem and which was known to both the forward finite-element simulation and SenseNet. At the right end, a moment, achieved by a distributive traction $F_x = 0.5 - z$, was imposed in the forward finite-element simulation, which remained unknown to SenseNet. Owing to the complexity of 3D modeling, sensors were distributed on the front, rear, top, and bottom surfaces to collect strain information on both the x-y and x-z planes. On each of these four surfaces, nine sensor pairs were assumed to be located at equally spaced intervals at the intersections of $x = \{1.25, 2.5, 3.75\}$ and y or $z = \{0.25, 0.5, 0.75\}$. Hence, a total of 36 sensor pairs were assumed to be attached to the beam. The orientations of the sensor pairs on each surface differed from those of their neighboring pairs, to collect more-diverse strain information.

Fig. 7 plots the SenseNet predictions of the 3D bending test results and the finite-element solution. The first and second columns show the contour plots of u_{mag} , u_x , u_y , and u_z on the deformed shape computed by the forward finite-element simulation and SenseNet, respectively. The deformed shapes are scaled by a factor of 10 for better visualization. The SenseNet prediction

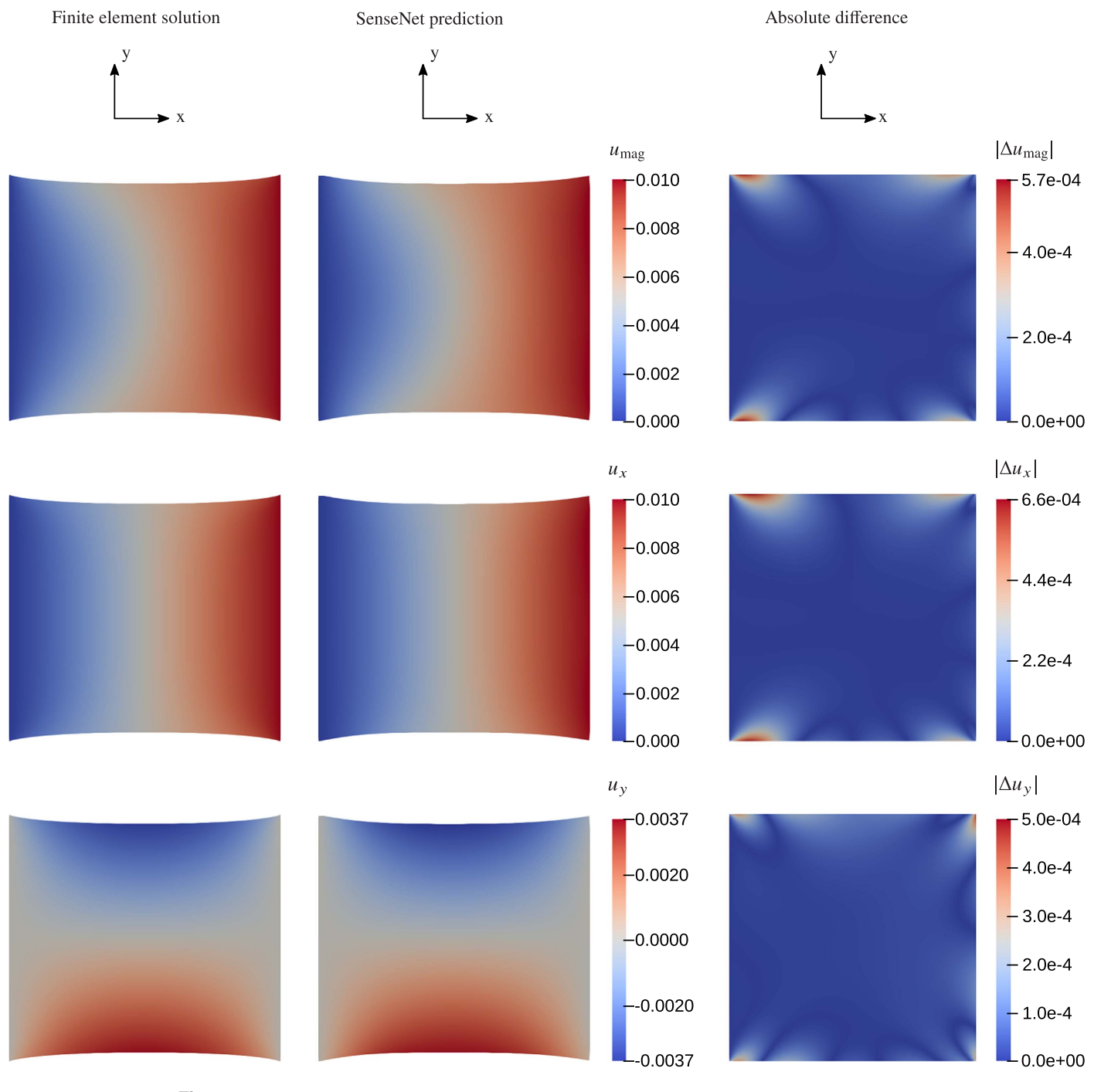


Fig. 6. Comparison of SenseNet prediction with finite-element solution for 2D fixed tension test.

matched well with the finite-element solution. The last column plots the absolute differences in $u_{\rm mag}$, u_x , u_y , and u_z between the finite-element solution and the SenseNet prediction on the undeformed shape. The maximal absolute differences $|\Delta u_{\rm mag}|$, $|\Delta u_x|$, $|\Delta u_y|$, and $|\Delta u_z|$, which mostly were located at the right end due to the unknown loading condition in SenseNet, were all of the same order of magnitude, 10^{-3} . The maximal PDs were about 6.4% in $u_{\rm mag}$, 6.8% in u_x , 100%, in u_y and 6.3% in u_z . In this problem, u_y mainly resulted from the Poisson effect, and therefore the magnitude of u_y was much smaller than the magnitude of other displacements, which further led to the largest maximal PD in u_y . The normalized RMSE was 1.97% for this problem (Table 2). Although the small transverse displacement

was not well captured by the model using just 72 sensor strain data, the small value of the holistic RMSE shows that SenseNet can capture the overall deformed shapes for the case of 3D bending reasonably well.

Three-Dimensional Fixed Tension Test

This subsection extends the 2D fixed tension test in the previous section into a 3D context by converting the unit square into a unit cube within (0,0,0) and (1,1,1). The boundary conditions included clamping left surface of the unit cube $(u_x = u_y = u_z = 0)$, which was known to both the forward finite-element simulation and SenseNet. In addition, the right surface of the cube was imposed

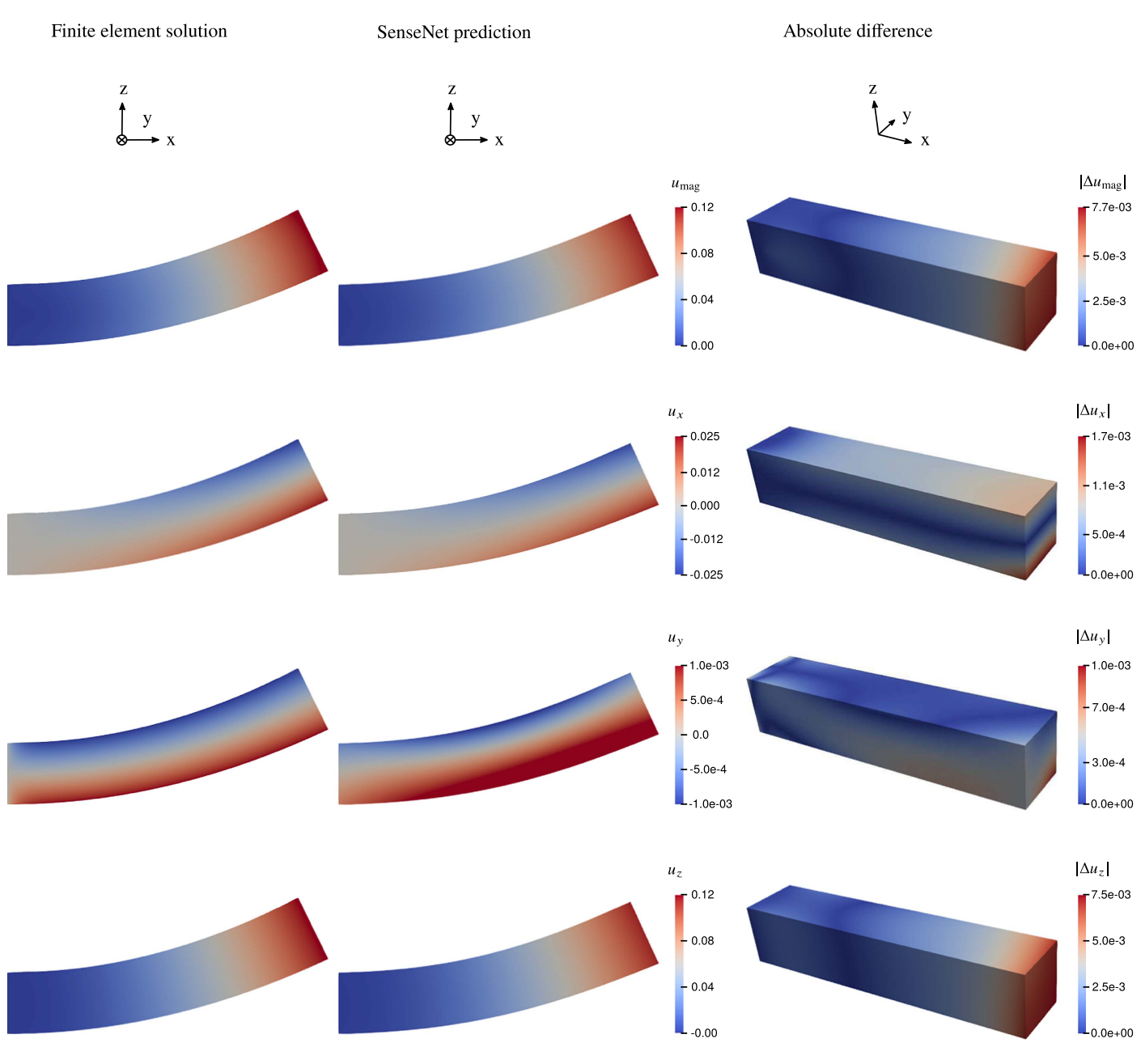


Fig. 7. Comparison of SenseNet prediction with finite-element solution for 3D bending test.

with a loading condition $u_x = 0.01$ and $u_y = u_z = 0$ in the forward finite-element simulation, which remained unknown to SenseNet. One can expect stress concentrations around the eight corners of the cube analogous to those in the 2D fixed tension test. To collect more sensor information from different surfaces, 36 sensor pairs were assumed at the intersections of $x = \{0.25, 0.5, 0.75\}$ and y

Table 2. Normalized RMSE and maximal PDs of 3D bending and fixed tension tests (%)

Problems	3D bending	3D fixed tension
Normalized RMSE	1.97	4.19
Maximal PD (u_{mag})	6.4	7.5
Maximal PD (u_x)	6.8	8.0
Maximal PD (u_y)	100.0	27.0
Maximal PD (u_z)	6.3	24.8

or $z = \{0.25, 0.5, 0.75\}$ on the front, rear, top, and bottom surfaces [Fig. 3(d)]. The sensor pairs on each surface had different orientations than their neighbors.

Fig. 8 plots the 3D fixed tension results computed by the forward finite-element simulation and predicted by SenseNet. For better visualization of the complete deformation of the cube, the deformations in both the x-y and x-z planes are presented, and all the deformed shapes are scaled by a factor of 10. The first two columns contain the contours of $u_{\rm mag}$, u_x , u_y , and u_z obtained by the finite-element method on the deformed shape. The SenseNet predictions of $u_{\rm mag}$, u_x , u_y , and u_z are plotted on the deformed shape in the middle two columns. The absolute differences in $u_{\rm mag}$, u_x , u_y , and u_z between the finite-element solution and SenseNet prediction are plotted on the undeformed shape in the last column. The SenseNet prediction matched the finite-element solution well. The absolute differences had the same order of magnitude, 10^{-4} . In the contour plots, the maximal absolute

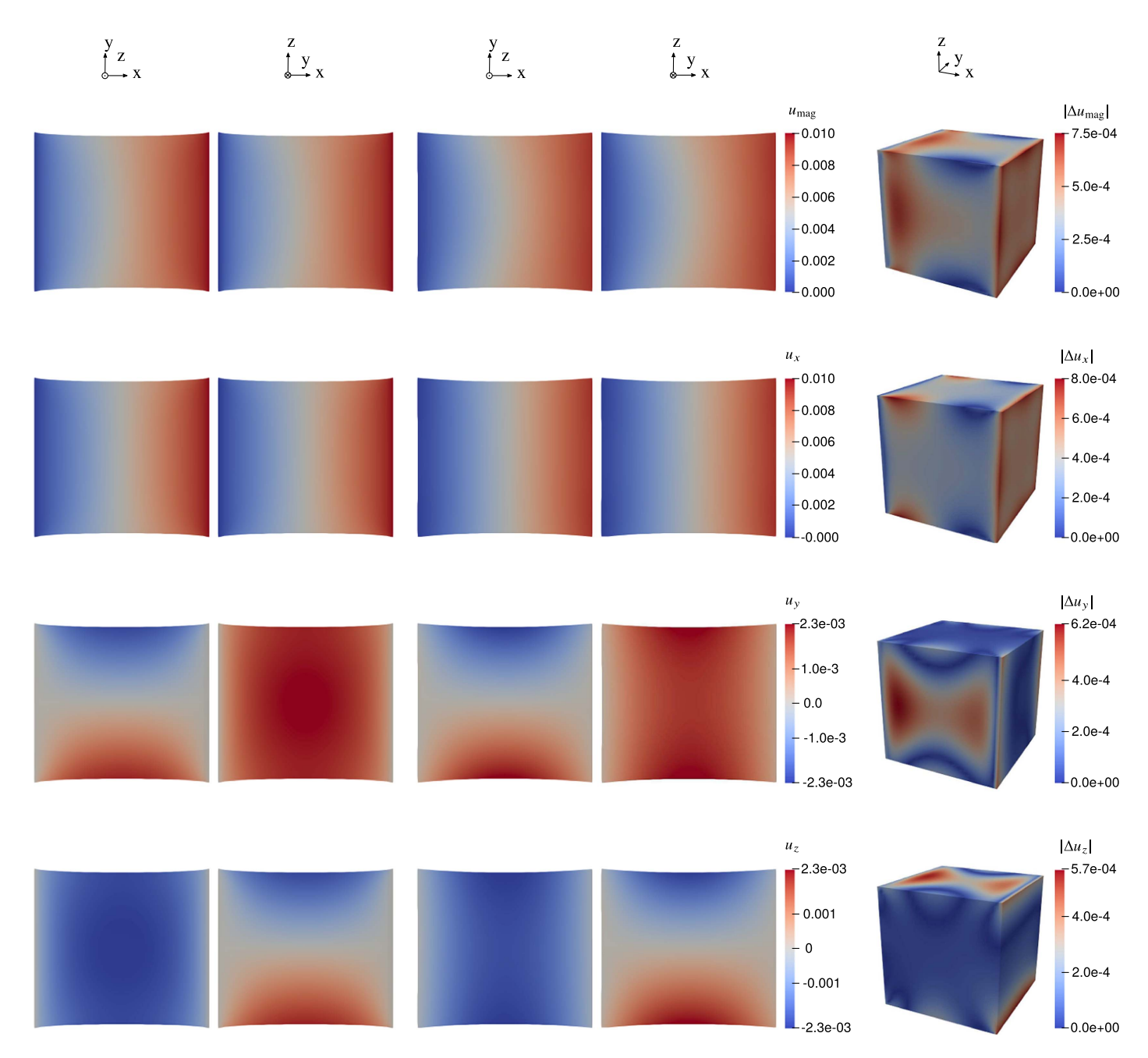


Fig. 8. Comparison of SenseNet prediction with finite-element solution for 3D fixed tension test.

differences occurred more around the boundary lines of the left (x=0) and right (x=1) surfaces, where stress concentrations arose. The maximal PDs were about 7.5% in $u_{\rm mag}$, 8.0% in u_x , 27.0% in u_y , and 24.8% in u_z . The maximal PD in u_x occurred mainly at the x=1 boundary because SenseNet did not have any information, either in terms of boundary conditions or surface sensor strain data, about that face (Fig. 8). The maximal PDs in u_y and u_z were much larger than those in u_x and $u_{\rm mag}$ due to their smaller values, because the main deflection of this problem was along the x-axis. The normalized RMSE was 4.19% for this problem (Table 2).

Although 3D applications present a challenge due to the unavailability of strain information inside the volume, these

numerical results validate the ability of our model to reconstruct the deformed shapes using just the surface sensor data with reasonable accuracy.

Sensor Density Effects

In addition to the neural network parameters which can be tuned, a few other factors, such as sensor density, directions, and locations, can impact the accuracy of the results. Practically, sensor directions and locations can be problem-specific. However, in all the examples in this study, we assumed a consistent strategy, wherein sensor directions can capture strain information along

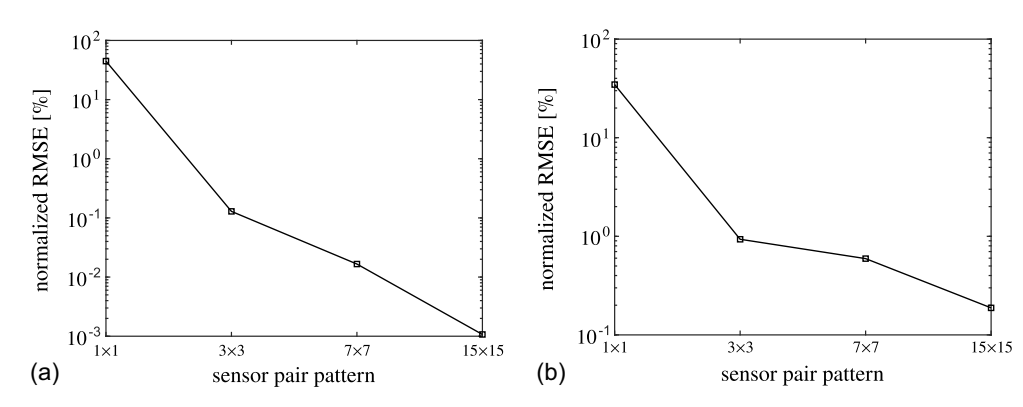


Fig. 9. Plots of the normalized RMSE versus the sensor pair pattern $(n_x \times n_y)$ studies: (a) 2D bending test; and (b) 2D fixed tension test.

four directions (0°, 45°, 90°, and 135°), and the locations are chosen for a uniform pattern of sensors. This strategy not only is experimentally feasible for fabrication, but also can be adopted across different problems with insignificant effects on the results. A major factor that can affect the resource cost of experiments and the accuracy of the SenseNet predictions is the amount of sensor data required. Therefore, this section discusses the effects of sensor density on the accuracy of SenseNet. The 2D bending and the 2D fixed tension tests with varying number of sensor pairs were considered for the discussion. The normalized RMSE was used as the metric for evaluating the accuracy of the predicted results.

In both the tests, four representative cases with different numbers of sensor pairs $(1 \times 1, 3 \times 3, 7 \times 7, \text{ and } 15 \times 15)$ were studied. All the sensors were spaced equally within the domain $[(0,0)\times(5,1)]$ for the bending test and $(0,0)\times(1,1)$ for the fixed tension test] in each case.

The normalized RMSE decreased with an increase in the number of sensors (Fig. 9). Due to the nonlinear nature of the neural network, a larger amount of sensor data results in higher accuracy of the predictions. Because a larger number of sensors contributes to additional financial costs and mechanical efforts for fabrication, an optimal and practical sensor pair pattern 3×3 , was utilized in all the simulations of this study. The results show that this minimal amount of data was sufficient for reconstructing the deformed shapes within an error tolerance of 1%, which is acceptable for most practical purposes. Furthermore, this study shows that although our model is reasonably accurate with a 3×3 sensor pair pattern, a larger amount of data potentially can improve its precision.

Conclusions

Shape sensing is an emerging technique with many interdisciplinary applications. Hence, a model for recapturing the deformed shapes using data from a discrete network of strain sensors and having widespread applicability to even thick 3D volumes is indispensable. This study proposes SenseNet, a physics-informed deep learning model, which predicts the displacement vector as the output corresponding to the input spatial position vector, for such applications. SenseNet consists of a fully connected neural network and a physics part which incorporates the prior knowledge of the problem. In the physics part, automatic differentiation is utilized to compute the mechanical strain and the governing equation residual information, using physics relations such as the strain–displacement relation, material constitutive

equation, and the law of balance of linear momentum. The loss function is assumed to consist of the error due to fulfillment of fixed boundary conditions, the error due to difference in the sensor strain data and predicted strains, and the error in satisfying the governing equation. The incorporation of these prior knowledge of the problem into the loss function is instrumental in making SenseNet physics-informed, and thus more robust than the existing conventional neural network approaches, which are biased depending on the choice of training data. SenseNet was validated using data generated from finite-element simulations for bending and fixed tension tests, in both 2D and 3D contexts. The normalized RMSEs obtained for the 2D bending and fixed tension tests and their 3D counterparts were 0.128%, 0.934%, 1.97%, and 4.19%, respectively. The fixed tension tests had larger normalized RMSEs than the bending tests mostly due to the occurrence of the stress concentrations. Due to the lack of strain information within the volume, the errors for the 3D tests were much larger than their 2D counterparts. Overall, the results corroborate the capability of our model to reconstruct the deformed shapes with reasonable accuracy using discrete strain sensor data. The study of the sensor density effects showed that the accuracy of the model can be improved with larger amounts of strain data.

Because SenseNet is a mesh-free method, it can be applicable to more-complex geometries. Due to the incorporation of the general 3D governing equation, the model is able to capture volume deformation using just the surface sensor data. Hence, unlike most existing models, SenseNet is not specialized for certain types of elements only, but can be applied universally to thick bodies as well. In the future, studies considering realistic complex applications and noise in sensor information are essential to prove the practicability of SenseNet. A study of the computational efficiency of the proposed model compared with other discretization methods also would be worthy future research work. The extension of the model for dynamic loading cases would be an interesting study for real-time shape sensing applications. Moreover, transfer learning can be promising in the generalization of reconstruction with respect to various deformations and structures (Lejeune and Zhao 2021).

Data Availability Statement

Some data, models, or code (e.g., finite-element and SenseNet results) that support the findings of this study are available from the corresponding author upon reasonable request.

Acknowledgments

Financial support for this research was provided by the US National Science Foundation under Contract No. CMMI-1911836 and by the Stanford UPS Endowment Fund.

References

- Arcadius Tokognon, C., B. Gao, G. Y. Tian, and Y. Yan. 2017. "Structural health monitoring framework based on Internet of Things: A survey." *IEEE Internet Things J.* 4 (3): 619–635. https://doi.org/10.1109/JIOT .2017.2664072.
- Bahmani, B., and W. Sun. 2021. "Training multi-objective/multi-task collocation physics-informed neural network with student/teachers transfer learnings." Preprint, submitted July 24, 2021. https://arxiv.org/abs/2107.11496.
- Bakalyar, J., and C. Jutte. 2012. "Validation tests of fiber optic strain-based operational shape and load measurements." In Proc., 53rd AIAA/ASME/ ASCE/AHS/ASC Structures, Structural Dynamics and Materials Conf. Reston, VA: American Institute of Aeronautics and Astronautics.
- Baydin, A. G., B. A. Pearlmutter, A. A. Radul, and J. M. Siskind. 2018. "Automatic differentiation in machine learning: A survey." J. Mach. Learn. Res. 18 (153): 1–43.
- Bogert, P., E. Haugse, and R. Gehrki. 2003. "Structural shape identification from experimental strains using a modal transformation technique." In *Proc.*, 44th AIAA/ASME/ASCE/AHS/ASC Structures, Structural Dynamics, and Materials Conf. Reston, VA: American Institute of Aeronautics and Astronautics.
- Brownjohn, J. M. W. 2007. "Structural health monitoring of civil infrastructure." *Philos. Trans. R. Soc. A* 365 (1851): 589–622. https://doi.org/10.1098/rsta.2006.1925.
- Bruno, R., N. Toomarian, and M. Salama. 1994. "Shape estimation from incomplete measurements: A neural-net approach." Smart Mater. Struct. 3 (2): 92–97. https://doi.org/10.1088/0964-1726/3/2/002.
- Cai, S., Z. Mao, Z. Wang, M. Yin, and G. E. Karniadakis. 2022. "Physics-informed neural networks (pinns) for fluid mechanics: A review." *Acta Mech. Sin.* 37 (12): 1727–1738. https://doi.org/10.1007/s10409-021-01148-1.
- Cai, S., Z. Wang, S. Wang, P. Perdikaris, and G. E. Karniadakis. 2021. "Physics-informed neural networks for heat transfer problems." *J. Heat Transfer* 143 (6): 060801. https://doi.org/10.1115/1.4050542.
- Castro-Toscano, M. J., J. C. Rodríguez-Quiñonez, O. Sergiyenko, W. Flores-Fuentes, L. R. Ramírez-Hernández, D. Hernández-Balbuena, L. Lindner, and R. Rascón. 2021. "Novel sensing approaches for structural deformation monitoring and 3D measurements." *IEEE Sens. J.* 21 (10): 11318–11328. https://doi.org/10.1109/JSEN.2020.3031882.
- Cerracchio, P., M. Gherlone, M. Di Sciuva, and A. Tessler. 2013. "Shape and stress sensing of multilayered composite and sandwich structures using an inverse finite element method." In *Proc.*, 5th Int. Conf. on Computational Methods for Coupled Problems in Science and Engineering (2013). Sarajevo, Bosnia: European Community on Computational Methods in Applied Sciences.
- Cerracchio, P., M. Gherlone, M. Di Sciuva, and A. Tessler. 2015. "A novel approach for displacement and stress monitoring of sandwich structures based on the inverse finite element method." *Compos. Struct.* 127 (Sep): 69–76. https://doi.org/10.1016/j.compstruct.2015.02.081.
- Davis, M. A., A. D. Kersey, J. Sirkis, and E. J. Friebele. 1996. "Shape and vibration mode sensing using a fiber optic Bragg grating array." Smart Mater. Struct. 5 (6): 759–765. https://doi.org/10.1088/0964-1726/5 /6/005.
- Dervilis, N., K. Worden, and E. Cross. 2015. "On robust regression analysis as a means of exploring environmental and operational conditions for SHM data." *J. Sound Vib.* 347 (Jul): 279–296. https://doi.org/10.1016/j.jsv.2015.02.039.
- Feng, D., and M. Q. Feng. 2018. "Computer vision for shm of civil infrastructure: From dynamic response measurement to damage detection— A review." Eng. Struct. 156 (Feb): 105–117. https://doi.org/10.1016/j .engstruct.2017.11.018.

- Fernando, G. F. 2005. "Fibre optic sensor systems for monitoring composite structures." *Reinf. Plast.* 49 (11): 41–49. https://doi.org/10.1016/S0034-3617(05)70836-5.
- Foss, G. C., and E. D. Haugse. 1995. "Using modal test results to develop strain to displacement transformations." In *Proc.*, 13th Int. Modal Analysis Conf. Bethel, CT: Society of Experimental Mechanics.
- Gherlone, M., P. Cerracchio, and M. Mattone. 2018. "Shape sensing methods: Review and experimental comparison on a wing-shaped plate." *Prog. Aerosp. Sci.* 99 (May): 14–26. https://doi.org/10.1016/j .paerosci.2018.04.001.
- Gherlone, M., P. Cerracchio, M. Mattone, M. Di Sciuva, and A. Tessler. 2012. "Shape sensing of 3d frame structures using an inverse finite element method." *Int. J. Solids Struct.* 49 (22): 3100–3112. https://doi.org/10.1016/j.ijsolstr.2012.06.009.
- Gherlone, M., P. Cerracchio, M. Mattone, M. Di Sciuva, and A. Tessler. 2014. "An inverse finite element method for beam shape sensing: Theoretical framework and experimental validation." *Smart Mater. Struct.* 23 (4): 045027. https://doi.org/10.1088/0964-1726/23/4/045027.
- Giurgiutiu, V. 2016. Structural health monitoring of aerospace composites.

 Oxford: Academic Press.
- Huang, B., and J. Wang. 2022. "Applications of physics-informed neural networks in power systems—A review." *IEEE Trans. Power Syst.* 1. https://doi.org/10.1109/TPWRS.2022.3162473.
- Ji, W., W. Qiu, Z. Shi, S. Pan, and S. Deng. 2021. "Stiff-PINN: Physics-informed neural network for stiff chemical kinetics." J. Phys. Chem. A 125 (36): 8098–8106. https://doi.org/10.1021/acs.jpca.1c05102.
- Jo, B. W., R. M. A. Khan, and Y.-S. Lee. 2018. "Hybrid blockchain and internet-of-things network for underground structure health monitoring." Sensors 18 (12): 4268. https://doi.org/10.3390/s18124268.
- Jutte, C. V., W. L. Ko, C. A. Stephens, J. A. Bakalyar, W. L. Richards, and A. R. Parker. 2011. Deformed shape calculation of a full-scale wing using fiber optic strain data from a ground loads test. Washington, DC: National Aeronautics and Space Administration.
- Kashinath, K., et al. 2021. "Physics-informed machine learning: Case studies for weather and climate modeling." *Philos. Trans. R. Soc. London*, Ser. A 379 (2194): 20200093. https://doi.org/10.1098/rsta.2020.0093.
- Kefal, A., and E. Oterkus. 2015. "Structural health monitoring of marine structures by using inverse finite element method." Anal. Des. Mar. Struct. V 341–349.
- Kefal, A., and E. Oterkus. 2016a. "Displacement and stress monitoring of a chemical tanker based on inverse finite element method." *Ocean Eng.* 112 (Jan): 33–46. https://doi.org/10.1016/j.oceaneng.2015.11.032.
- Kefal, A., and E. Oterkus. 2016b. "Displacement and stress monitoring of a Panamax containership using inverse finite element method." *Ocean Eng.* 119 (Jun): 16–29. https://doi.org/10.1016/j.oceaneng.2016 .04.025.
- Kefal, A., E. Oterkus, A. Tessler, and J. L. Spangler. 2016. "A quadrilateral inverse-shell element with drilling degrees of freedom for shape sensing and structural health monitoring." *Eng. Sci. Technol. Int. J.* 19 (3): 1299–1313. https://doi.org/10.1016/j.jestch.2016.03.006.
- Kefal, A., I. E. Tabrizi, M. Yildiz, and A. Tessler. 2021. "A smoothed ifem approach for efficient shape-sensing applications: Numerical and experimental validation on composite structures." *Mech. Syst. Sig. Process*. 152 (May): 107486. https://doi.org/10.1016/j.ymssp.2020.107486.
- Kefal, A., A. Tessler, and E. Oterkus. 2017. "An enhanced inverse finite element method for displacement and stress monitoring of multilayered composite and sandwich structures." *Compos. Struct.* 179 (Nov): 514–540. https://doi.org/10.1016/j.compstruct.2017.07.078.
- Kefal, A., and M. Yildiz. 2017. "Modeling of sensor placement strategy for shape sensing and structural health monitoring of a wing-shaped sandwich panel using inverse finite element method." Sensors 17 (12): 2775. https://doi.org/10.3390/s17122775.
- Kim, N.-S., and N. Cho. 2004. "Estimating deflection of a simple beam model using fiber optic bragg-grating sensors." *Exp. Mech.* 44 (4): 433–439. https://doi.org/10.1007/BF02428097.
- Ko, W., and V. Fleischer. 2009. Further development of Ko displacement theory for deformed shape predictions of nonuniform aerospace structures. Washington, DC: National Aeronautics and Space Administration.

- Ko, W., W. L. Richards, and V. Fleischer. 2009. Applications of Ko displacement theory to the deformed shape predictions of the doubly-tapered Ikhana wing. Washington, DC: National Aeronautics and Space Administration
- Ko, W., W. L. Richards, and V. Tran. 2007. Displacement theories for in-flight deformed shape predictions of aerospace structures. Washington, DC: National Aeronautics and Space Administration.
- Kumar, M., S. Rappo, L. Facchini, and M. Tomaselli. 2022. "Translation of three-dimensional printing for orthopedic devices." MRS Bull. 47 (1): 49–58. https://doi.org/10.1557/s43577-021-00262-6.
- Lejeune, E., and B. Zhao. 2021. "Exploring the potential of transfer learning for metamodels of heterogeneous material deformation." *J. Mech. Behav. Biomed. Mater.* 117 (May): 104276. https://doi.org/10.1016/j.imbbm.2020.104276.
- Li, W., M. Z. Bazant, and J. Zhu. 2021. "A physics-guided neural network framework for elastic plates: Comparison of governing equations-based and energy-based approaches." *Comput. Methods Appl. Mech. Eng.* 383 (Sep): 113933. https://doi.org/10.1016/j.cma.2021.113933.
- Liang, S., C. Zhang, W. Lin, L. Li, C. Li, X. Feng, and B. Lin. 2009. "Fiber-optic intrinsic distributed acoustic emission sensor for large structure health monitoring." *Opt. Lett.* 34 (12): 1858–1860. https://doi.org/10.1364/OL.34.001858.
- Linka, K., A. Schafer, X. Meng, Z. Zou, G. E. Karniadakis, and E. Kuhl. 2022. "Bayesian physics-informed neural networks for real-world nonlinear dynamical systems." Preprint, submitted May 12, 2022. https:// arxiv.org/abs/2205.08304.
- Liu, X., S. Tian, F. Tao, and W. Yu. 2021. "A review of artificial neural networks in the constitutive modeling of composite materials." *Composites, Part B* 224 (Nov): 109152. https://doi.org/10.1016/j.compositesb.2021.109152.
- Lucor, D., A. Agrawal, and A. Sergent. 2021. "Physics-aware deep neural networks for surrogate modeling of turbulent natural convection." Preprint, submitted March 5, 2021. https://arxiv.org/abs/2103.03565.
- Mahmoudabadbozchelou, M., M. Caggioni, S. Shahsavari, W. H. Hartt, G. Em Karniadakis, and S. Jamali. 2021a. "Data-driven physics-informed constitutive metamodeling of complex fluids: A multifidelity neural network (MFNN) framework." J. Rheol. 65 (2): 179–198. https://doi.org/10 .1122/8.0000138.
- Mahmoudabadbozchelou, M., G. E. Karniadakis, and S. Jamali. 2021b. "nn-PINNs: Non-newtonian physics-informed neural networks for complex fluid modeling." Soft Matter 18 (1): 172–185. https://doi.org/10.1039/D1SM01298C.
- Mao, Z., and M. Todd. 2008. "Comparison of shape reconstruction strategies in a complex flexible structure." In Vol. 6932 of Sensors and smart structures technologies for civil, mechanical, and aerospace systems 2008, 127–138. Bellingham: International Society for Optics and Photonics, SPIE.
- Pisoni, A. C., C. Santolini, D. E. Hauf, and S. Dubowsky. 1995. "Displacements in a vibrating body by strain gauge measurements." In *Proc.*, 13th Int. Conf. on Modal Analysis. Bethel, CT: Society of Experimental Mechanics.
- Quach, C. C., S. L. Vazquez, A. Tessler, J. P. Moore, E. G. Cooper, and J. L. Spangler. 2005. "Structural anomaly detection using fiber optic sensors and inverse finite element method." In *Proc., AIAA Guidance, Navigation, and Control Conf. and Exhibit*. Reston, VA: American Institute of Aeronautics and Astronautics.
- Raissi, M., P. Perdikaris, and G. Karniadakis. 2019. "Physics-informed neural networks: A deep learning framework for solving forward

- and inverse problems involving nonlinear partial differential equations." *J. Comput. Phys.* 378 (Feb): 686–707. https://doi.org/10.1016/j.jcp.2018.10.045.
- Rao, C., L. Tian, D.-M. Yan, S. Liao, O. Deussen, and L. Lu. 2019. "Consistently fitting orthopedic casts." *Comput. Aided Geom. Des.* 71 (May): 130–141. https://doi.org/10.1016/j.cagd.2019.04.018.
- Sahli Costabal, F., Y. Yang, P. Perdikaris, D. E. Hurtado, and E. Kuhl. 2020. "Physics-informed neural networks for cardiac activation mapping." Front. Phys. 8 (Feb): 42. https://doi.org/10.3389/fphy.2020.00042.
- Shen, W., R. Yan, L. Xu, G. Tang, and X. Chen. 2015. "Application study on FBG sensor applied to hull structural health monitoring." *Optik* 126 (17): 1499–1504. https://doi.org/10.1016/j.ijleo.2015.04.046.
- Sun, L., and J.-X. Wang. 2020. "Physics-constrained bayesian neural network for fluid flow reconstruction with sparse and noisy data." *Theor. Appl. Mech. Lett.* 10 (3): 161–169. https://doi.org/10.1016/j.taml.2020.01.031.
- Tessler, A., M. Di Sciuva, and M. Gherlone. 2010. "A consistent refinement of first-order shear deformation theory for laminated composite and sandwich plates using improved zigzag kinematics." *J. Mech. Mater. Struct.* 5 (2): 341–367. https://doi.org/10.2140/jomms.2010.5.341.
- Tessler, A., and J. L. Spangler. 2003. A variational principle for reconstruction of elastic deformations in shear deformable plates and shells. Hampton, VA: Langley Research Center.
- Tessler, A., and J. L. Spangler. 2004. "Inverse fem for full-field reconstruction of elastic deformations in shear deformable plates and shells." In *Proc.*, 2nd European Workshop on Structural Health Monitoring. Toronto, ON, Canada: DEStech.
- Tessler, A., and J. L. Spangler. 2005. "A least-squares variational method for full-field reconstruction of elastic deformations in shear-deformable plates and shells." *Comput. Methods Appl. Mech. Eng.* 194 (2): 327–339. https://doi.org/10.1016/j.cma.2004.03.015.
- Tessler, A., J. L. Spangler, M. Gherlone, M. Mattone, and M. D. Sciuva. 2011. "Real-time characterization of aerospace structures using onboard strain measurement technologies and inverse finite element method." In *Proc.*, 8th Int. Workshop on Structural Health Monitoring, 981–988. Stanford, CA: IWSHM.
- Xiang, J.-W., Z.-B. Yang, and J. L. Aguilar. 2018. "Structural health monitoring for mechanical structures using multi-sensor data." *Int. J. Distrib. Sens. Netw.* 14 (9): 155014771880201. https://doi.org/10.1177/1550147718802019.
- Yang, E. S., N. Aslani, and A. McGarry. 2019. "Influences and trends of various shape-capture methods on outcomes in trans-tibial prosthetics: A systematic review." *Prosthet. Orthot. Int.* 43 (5): 540–555. https://doi.org/10.1177/0309364619865424.
- Zhang, E., M. Yin, and G. E. Karniadakis. 2020a. "Physics-informed neural networks for nonhomogeneous material identification in elasticity imaging." Preprint, submitted September 2, 2020. https://arxiv.org/abs/2009.04525.
- Zhang, Q., Y. Chen, Z. Yang, and E. Darve. 2020b. "Multi-constitutive neural network for large deformation poromechanics problem." Preprint, submitted October 11, 2020. https://arxiv.org/abs/2010.15549.
- Zhang, X., and K. Garikipati. 2021. "Bayesian neural networks for weak solution of PDEs with uncertainty quantification." Preprint, submitted January 13, 2021. https://arxiv.org/abs/2101.04879.
- Zhao, F., L. Xu, H. Bao, and J. Du. 2020. "Shape sensing of variable cross-section beam using the inverse finite element method and isogeometric analysis." *Measurement* 158 (Jul): 107656. https://doi.org/10.1016/j.measurement.2020.107656.